Astronomy & Astrophysics manuscript no. output
May 6, 2026

4MOST ChANGES: Catalog of high-redshift quasar candidates ($4.5 < z < 7$) selected via spectral-energy-distribution fitting

Tatevik Mkrtchyan (Տաթևիկ Մկրտչյան)[1], Chiara Mazzucchelli[1], Roberto J. Assef[1], Matthew J. Temple[2], Alejandra Rojas-Lilayú[3], Franz E. Bauer[4], Victoria Toptun[5], J. A. Acevedo Barroso[14], Silvia Belladitta[7,8], Emanuele Paolo Farina[8,9], L. N. Martínez-Ramírez[6,10,11], Giulia Papini[8,12], Sarath Satheesh-Sheeba[13], Daniel Stern[14], and Anuraag Upadhyayula[15]

[1] Instituto de Estudios Astrofísicos, Universidad Diego Portales, Av. Ejército Libertador 441, Santiago, Chile
[2] Centre for Extragalactic Astronomy, Department of Physics, Durham University, South Road, Durham DH1 3LE, United Kingdom
[3] Universidad Técnica Federico Santa María, Av. Vicuña Mackenna 3939, 8940897 San Joaquín, Santiago, Chile
[4] Instituto de Alta Investigación, Universidad de Tarapacá, Casilla 7D, Arica, Chile
[5] European Southern Observatory, Karl Schwarzschildstrasse 2, 85748, Garching bei München, Germany
[6] Instituto de Astrofísica, Facultad de Física, Pontificia Universidad Católica de Chile Av. Vicuña Mackenna 4860, 7820436 Macul, Santiago, Chile
[7] Max-Planck-Institut für Astronomie, Königstuhl 17, D-69117, Heidelberg, Germany
[8] INAF, Osservatorio di Astrofisica e Scienza dello Spazio (OAS), Via Gobetti 93/3, 40129 Bologna, Italy
[9] International Gemini Observatory/NSF NOIRLab, 670 N A'ohoku Place, Hilo, Hawai'i 96720, USA
[10] Fakultät für Physik und Astronomie, Universität Heidelberg, Im Neuenheimer Feld 226, 69120 Heidelberg, Germany
[11] Millennium Institute of Astrophysics (MAS), Nuncio Monseñor Sótero Sanz 100, Providencia, Santiago, Chile
[12] Dipartimento di Fisica e Astronomia "Augusto Righi", Alma Mater Studiorum - Università di Bologna, via Gobetti 93/2, 40129 Bologna, Italy
[13] Instituto de Astrofísica, Facultad de Ciencias Exactas, Universidad Andrés Bello, Fernández Concha 700, 7591538 Las Condes, Santiago, Chile
[14] Jet Propulsion Laboratory, California Institute of Technology, 4800 Oak Grove Drive, Pasadena, CA 91109, USA
[15] University of Missouri–Kansas City, Kansas City, MO 64110, USA

Accepted 9 April 2026

ABSTRACT

Context. The identification of high-redshift quasars ($z > 4.5$) is critical for studying the early Universe, supermassive-black-hole growth, and cosmic reionization. Most known high-redshift quasars are located in the northern hemisphere, leaving the southern sky largely unexplored.

Aims. As part of the 4-meter Multi-Object Spectroscopic Telescope (4MOST) and Chilean AGN/Galaxy Extragalactic Survey (ChANGES) S1604 survey, we aim to create a large catalog of high-redshift quasar candidates in the southern hemisphere using multiwavelength photometry and spectral-energy-distribution (SED) fitting, with the goal of spectroscopic follow-up with 4MOST.

Methods. We constructed a multiband photometric catalog by combining optical data from the Dark Energy Camera Local Volume Exploration Survey (DELVE DR2) and Dark Energy Camera Legacy Survey (DECaLS DR10), near-infrared data from the VISTA Hemisphere Survey (VHS DR5) with an additional field of the VISTA Kilo-degree Infrared Galaxy Public Survey (VIKING), mid-infrared data from the Wide-field Infrared Survey Explorer (AllWISE), and optical astrometry from Gaia DR3. After applying morphological and color-based cuts to remove contaminants such as brown dwarfs and red galaxies, we performed a custom-made SED fitting using quasar and brown-dwarf templates. Statistical outputs including χ^2, the Bayesian information criterion (BIC), and $F_{\rm test}$ were used to rank and select candidates.

Results. Our final catalog contains 6104 high-redshift quasar candidates within the redshift range of $4.5 < z < 7$. These sources have detections in seven or more photometric bands and satisfy our SED-based statistical selection criteria (e.g., $BIC > 0$ and $F_{\rm test} > 10$). Initial spectroscopic validation using the New Technology Telescope (NTT) with the ESO Faint Object Spectrograph and Camera v.2 (EFOSC2) and the Palomar Observatory Hale Telescope with the Next Generation Palomar Spectrograph (NGPS) confirmed three high-redshift quasars at $z > 5$ out of six observed candidates.

Key words. galaxies:active – galaxies:high-redshift – galaxies:nuclei – quasars:general - quasars:photometry - catalogs

Article published by EDP Sciences, to be cited as https://doi.org/10.1051/0004-6361/202557171

1. Introduction

Quasars are the most luminous type of active galactic nuclei (AGN) powered by the accretion of material onto supermassive black holes (SMBHs) located at the centers of massive galaxies (e.g., Magorrian et al. 1998, Marconi & Hunt 2003). These powerful sources emit across the entire electromagnetic spectrum. They can be studied at large cosmological look-back times, with spectroscopically confirmed quasars now reaching redshifts of $z \sim 7.6$ (e.g., Bañados et al. 2018, Yang et al. 2020, Wang et al. 2021). Recent observations have also identified AGN candidates at even higher redshifts of $z \sim 10$ (about half a billion years after the Big Bang; e.g., Bogdán et al. 2024; Natarajan et al. 2024). Additionally, high-redshift quasars provide valuable information on the chemical composition and metal enrichment of the intergalactic medium (IGM; e.g., Becker et al. 2015, Bosman et al. 2022 and Davies et al. 2023) and highlight relatively dense environments (e.g., Mignoli et al. 2020, Pudoka et al. 2024, Lambert et al. 2024, Champagne et al. 2025a,b).

The discovery of the first quasars at $z > 4$ in the 1980s marked a significant milestone in our understanding of the distant Universe (e.g., Warren et al. 1987). The exploration of high-redshift quasars further accelerated with the advent of the Sloan Digital Sky Survey (SDSS; York et al. 2000), which led to the discovery of the first quasars at $z > 5$ (e.g., Fan et al. 2001). Since then, systematic wide-field surveys such as Wide-field Infrared Survey Explorer (WISE; Wright et al. 2010), the UKIRT Infrared Deep Sky Survey (UKIDSS; Lawrence et al. 2007), Gaia (Gaia Collaboration et al. 2016), and the Panoramic Survey Telescope and Rapid Response System (Pan-STARRS; Chambers et al. 2016), along with deep, multiwavelength observations of smaller fields such as COSMOS and the Chandra Deep Fields have significantly advanced the identification and characterization of AGNs and quasars beyond the local Universe (Brandt et al. 2001, Giacconi et al. 2002, Lehmer et al. 2005, Salvato et al. 2009, Marchesi et al. 2016). To date, more than 500 quasars have been identified at $z > 5.6$, the majority located in the northern hemisphere (Fan et al. 2023, Yang et al. 2024, Belladitta et al. 2025). These discoveries confirmed the existence of SMBHs with masses of up to a few billion solar masses ($M_\odot$) within the first billion years after the Big Bang, with rest-frame UV/optical spectra remarkably similar to those of luminous low-redshift quasars (e.g., Mazzucchelli et al. 2023, Farina et al. 2022). The field was recently revolutionized by the James Webb Space Telescope (JWST), which revealed new populations of faint, obscured high-redshift AGN candidates that were previously missed by traditional selection methods, specifically little red dots (LRDs), with number densities an order of magnitude higher than expected (e.g., Matthee et al. 2024, Kocevski et al. 2025).

Most high-redshift quasars have been identified using the Lyman-break (or dropout) technique (Warren et al. 1987, Williams et al. 1996). This method capitalizes on the absorption of flux below the Lyα emission line (at a rest-frame wavelength of 1215 Å) due to both the Lyman break and the Lyα forest from intervening absorption features, which together produce very red broadband colors. Early work on photometric quasar identification established color-based selection criteria (Richards et al. 2001, 2004) that have been continuously refined over two decades (Richards et al. 2015). The color-cut method is straightforward to implement and achieves high completeness, even for quasars with atypical spectra (Fan et al. 2023). However, this method often suffers from significant contamination due to the similar optical and near-infrared (NIR) colors of other astrophysical sources. Multiple stellar populations have similar colors to high-redshift quasars, including cool brown dwarfs with spectral types M, L, and T, low-mass stars, and compact early-type galaxies (e.g., Hewett et al. 2006, Findlay et al. 2012, Venemans et al. 2015, Bañados et al. 2016, Gloudemans et al. 2022, Belladitta et al. 2025, Ighina et al. 2025). Among these contaminants, cool brown dwarfs represent the dominant source of confusion in photometric surveys, outnumbering $z \sim 7$ quasars by two to four orders of magnitude in deep surveys (Euclid Collaboration et al. 2019), making them the primary challenge for color-based selection of high-redshift quasars.

To address these issues, several studies (e.g., Hatziminaoglou et al. 2004, Mortlock et al. 2012, Matsuoka et al. 2016 and Reed et al. 2017) applied spectral-energy-distribution (SED) fitting following the initial color cuts, calculating reduced χ^2 values by comparing observed SEDs to models of quasars and potential contaminants, including various M, L, and T dwarf types and early-type galaxies at different redshifts. These SED-fitting approaches have been refined with multiwavelength data over the years (Messias et al. 2012 and Findlay et al. 2012) and extended to higher redshifts (Nakoneczny et al. 2021), including recent searches for dust-reddened quasars at $z > 6$ (Iwamoto et al. 2025). More recently, the use of machine-learning techniques has facilitated the discovery of new high-redshift quasars, even in datasets that have previously undergone extensive searches (e.g., Wenzl et al. 2021, Yang et al. 2024, Byrne et al. 2024, Calderone et al. 2024).

In addition to northern hemisphere efforts such as SDSS (York et al. 2000) and Pan-STARRS (PS1; Chambers et al. 2016) that have enabled a drastic increase in the number of quasars discovered at $z > 4$ (e.g., Shen et al. 2011, Bañados et al. 2016, 2023, Jiang et al. 2016, Wang et al. 2016, Gloudemans et al. 2022, Belladitta et al. 2019 and Belladitta et al. 2023), several recent large-area surveys have expanded high-redshift quasar searches into the southern sky, such as the Dark Energy Survey (DES; Flaugher 2005, Abbott et al. 2018), the DESI Legacy Imaging Surveys (LS; Dey et al. 2019), and SkyMapper (Keller et al. 2007), which have enabled the discovery of high-redshift quasars in the southern hemisphere (e.g., Reed et al. 2017, Pons et al. 2019, Belladitta et al. 2019, Wolf et al. 2020, Onken et al. 2022, Yang et al. 2023, Ighina et al. 2023, 2025). However, the southern hemisphere still lacks the extensive spectroscopic coverage and time-domain infrastructure available in the north. This gap presents both a challenge and an opportunity for the next generation of extragalactic surveys (e.g., de Jong et al. 2019, Bauer et al. 2023).

Among the various astronomical facilities, the 4-meter Multi-Object Spectroscopic Telescope (4MOST) installed on the Visible and Infrared Survey Telescope for Astronomy (VISTA) at Paranal Observatory stands out as a key asset in the southern hemisphere, covering the sky in the declination range $-70^\circ < \mathrm{dec} < 5^\circ$ in the coming years (Guiglion et al. 2019). 4MOST can observe approximately 2,400 targets simultaneously across a wide field of view of 4.2 square degrees. Over its initial five-year survey, it is expected to obtain spectra for over 20 million sources at a

spectral resolution of $R \sim 6500$, and more than 3 million spectra at $R \sim 20,000$ (de Jong et al. 2019).

The 4MOST Chilean AGN/Galaxy Evolution Survey (ChANGES; Bauer et al. 2023) is one of 15 community surveys approved for 4MOST, allocated approximately 8.23% of the low-resolution spectrograph (LRS) fiber hours. ChANGES aims to obtain spectroscopy for ∼2.3 million AGN candidates spanning ∼18,000 square degrees, primarily selected through optical variability (using ZTF, La Silla QUEST, and Gaia data) and optical/NIR/mid-infrared (MIR) SED fitting. The survey's primary science goals include: (1) improving population statistics for moderate-luminosity and lower mass black-hole AGNs out to $z \sim 1$; (2) expanding the known AGN sample available to facilities such as the Vera C. Rubin Observatory's Legacy Survey of Space and Time (LSST; Ivezić et al. 2019), Euclid, and ESO's Extremely Large Telescope; (3) generating a massive training set for LSST/Euclid classification and photometric redshift calibration; (4) studying AGN spectral variability through multi-epoch observations of ∼200,000 variable-selected AGNs; and (5) investigating extreme variability events, tidal disruption events, and lensed AGNs through dedicated target-of-opportunity observations.

Among these goals, ChANGES dedicates effort to identifying high-redshift ($4.5 < z < 7$) quasar candidates in the southern hemisphere, particularly at the southernmost declinations (dec $< -30°$), which remain poorly explored. Our work aims to provide a catalog of high-redshift quasar candidates selected using a custom-made SED fitting code and applying several criteria outlined in the following sections. The paper is organized as follows. In Section 2, we describe the data used in this work. Section 3 explains the method of photometric selection and provides justification for the criteria applied. Section 4 presents the output of our catalog with the results obtained and the preliminary spectroscopic follow-up. Finally, we summarize our findings in Section 5. We used a flat Λ cold dark matter (ΛCDM) cosmology with $H_0 = 70$ km s^{-1} Mpc^{-1}, $\Omega_m = 0.30$, and $\Omega_\Lambda = 0.70$.

2. Photometric data

To ensure consistency across multiple ChANGES science cases, a single uniform photometric catalog was constructed, which includes $\sim 4.2 \times 10^8$ objects from the southern sky ($dec < 5°$). The catalog was created by cross-matching optical $griz$ photometry from the second public data release (DR2) of the Dark Energy Camera Local Volume Exploration Survey (DELVE; Drlica-Wagner et al. 2022), NIR $YJHK_s$ photometry from the fifth data release (DR5) of the VISTA Hemisphere Survey (VHS) with an additional field of the VISTA Kilo-degree Infrared Galaxy Public Survey (VIKING; Edge et al. 2013), and MIR $W1$ and $W2$ photometry from the CatWISE 2020 catalog (Marocco et al. 2021). The primary source detections are from DELVE DR2, with additional photometry cross-matched from VHS/VIKING and CatWISE when available. NIR gaps in the southern-sky coverage are supplemented by VIKING, which covers approximately $0° \lesssim RA \lesssim 50°$ and $-35° \lesssim dec \lesssim -10°$, addressing a major gap in VHS coverage. Additional gaps in VHS coverage, including several horizontal stripes at various declinations (most prominently at dec $\sim -5°$, $-15°$, $-30°$, and $-40°$) and scattered regions throughout the footprint, cannot be filled with NIR data. In these regions where NIR data from VHS/VIKING are unavailable, the catalog contains only optical and MIR photometry (DELVE+CatWISE). The different photometric depths between VHS (5σ limiting magnitudes: $J \sim 20.6$, $K_s \sim 18.5$; McMahon et al. 2013, 2021) and VIKING ($J \sim 21.2$, $K_s \sim 19.8$; Edge et al. 2013) may introduce systematic biases in candidate selection across different sky regions. Duplicate objects are removed using a $1''$ matching radius, consistent with the $1.4''$ diameter of the 4MOST fibers. Furthermore, this catalog incorporates proper-motion information and object-type flags from Gaia DR3 (Gaia Collaboration et al. 2023). In the following step of our selection, we additionally used magnitudes from the tenth data release (DR10) of the Dark Energy Camera Legacy Survey (DECaLS; Dey et al. 2019[1]), which are not included in our initial catalog as it was built to optimize sky coverage and consistency across all ChANGES science cases; hence, DELVE DR2 was chosen instead for the optical coverage (Assef, in prep; Bauer, in prep). We also used the Milky Way dust-reddening map, from Schlegel, Finkbeiner, and Davis (SFD; Schlegel et al. 1998) dust maps to obtain dust extinction values of $E(B-V)$. The catalog is divided into sections of 15° by right ascension (RA), each containing around 8 million to 20 million entries.

The Dark Energy Camera (DECam) is a 570-megapixel instrument mounted on the four-meter Victor M. Blanco Telescope at Cerro Tololo in Chile. Since its commissioning, DECam has served the DES, the DECaLS, and other community programs, capturing much of the southern sky. DELVE DR2 includes imaging from DELVE, DES, and DECaLS with a median 5σ point-source depth of $g = 24.3$, $r = 23.9$, $i = 23.5$, and $z = 22.8$ magnitudes (Drlica-Wagner et al. 2022), and covers nearly the entire southern hemisphere. In contrast, DECaLS DR10 has new i-band imaging plus grz. It incorporates DECaLS observations from 2014 to 2019 and additional DECam data from DES, DELVE, and DeROSITA surveys. DECaLS reaches depths of $g = 24.7$, $r = 23.9$, $z = 23.0$, referring to the target 5σ point-source depth, providing deeper g-band photometry that serves as a helpful alternative selection criterion for removing potential contaminants. However, DECaLS DR10 does not provide full sky coverage in the 4MOST-accessible area, with significant gaps particularly in the i and z bands, which is why DELVE DR2 served as our primary photometric source.

The VISTA Hemisphere Survey DR5 spans the entire southern celestial hemisphere ($dec < 0°$), covering 20,000 deg^2 and reaching depths 30 times fainter than those achieved by 2MASS/DENIS. This survey provides data for ∼ 1.4 billion detections, offering measurements across four NIR broadband filters such as Y, J, H, and Ks with AB depths of 21.1, 20.8, 20.5, and 20.0 (5σ), respectively (Pons et al. 2019). Similarly, VIKING covers 1500 deg^2 across two regions of the extragalactic sky using VISTA in the z, Y, J, H, and K_s bands to an AB depth of 23.1, 22.3, 22.1, 21.5, and 21.2, respectively, with the 5σ point-source depth (Edge et al. 2013). Lastly, we used the CatWISE 2020 Catalog, which combines two-band (3.4, 4.6) fluxes, positional data, apparent-motion measurements, and flux-variability statistics (Wright et al. 2010, Marocco et al. 2021).

In summary, our initial photometric catalog covers the full southern sky ($dec < 5°$) and contains $\sim 4.2 \times 10^8$

[1] https://www.legacysurvey.org/dr10/description/

objects with up to ten bands of DECam *griz*, VISTA $YJHK_s$, and WISE $W1/2$, spanning a wavelength range of ∼4800–46000 Å (optical to MIR). For magnitude measurements, we used Kron-like aperture photometry (`mag_auto`) for DELVE optical data, Petrosian photometry (`petromag`) for VHS/VIKING NIR data, and profile-fitting photometry (`mpro`) for CatWISE MIR data. All magnitudes are in the AB system unless otherwise stated. In addition to photometric data, some value-added (non-photometric) columns are used in the selection process. These are three Gaia-based parameters: proper motion if available and its uncertainties in RA and Dec, the *extended_class_z_delve* flag, and $E(B-V)$ values derived from SFD. The full catalog is divided into sections of 15 degrees by RA, with each segment containing around 8 million to 20 million entries, including three chunks with the gaps in VHS coverages. It is publicly available online[2].

3. Methodology

We imposed several initial selection criteria to identify high-redshift quasars at $z > 4.5$, followed by implementing a custom-made SED fitting code and color–color cuts. Finally, we cross-matched part of our sample with the DECaLS DR10 catalog to retrieve further information. Our selection procedure is reported schematically in Figure 1 and explained in more detail below.

3.1. Removing initial contaminants

Initially, we applied a set of conditions to remove contaminants. To test their effectiveness, we used three high-redshift quasar samples: F23 (a collection of around 500 spectroscopically confirmed quasars at redshifts $5.3 < z < 7.6$ from Fan et al. 2023), Y23 (a spectroscopically confirmed list of 556 quasars with redshift values between 4.4 and 6.6, based on DESI data from the study of Yang et al. 2023), and Fl23 (a list of high-redshift quasars from the study of Flesch 2023, totaling 1200 sources with $z > 4.5$, out of which we selected about 450 spectroscopically confirmed quasars). For comparison with known contaminants, we also used a spectroscopically confirmed sample of brown dwarfs from a collection of studies[3] (totaling 5,700 sources), hereafter referred to as the BD sample. All samples are cross-matched with the surveys adopted in this work. Note that the recovery rate includes sources that passed the selection criteria or those retained due to missing data (NaN values), which pass selection criteria by default.

High-redshift quasars are expected to be characterized by a point-like morphology. Since our sample focuses on sources at $z > 4.5$, we used the DELVE survey's *extended_class_z_delve* flag to distinguish point-like sources from extended ones (e.g., galaxies) based on their z-band morphology. Hence, we consider that any high-redshift quasar ($4.5 < z < 7$) candidates should be detected in the z_{delve} filter, and choose it as a reference for the morphology of the source. The *extended_class_z_delve* flag is based on morphological models based on the spread model parameter of *Source Extractor* (Bertin & Arnouts 1996) and has the following values: 0: source has a high

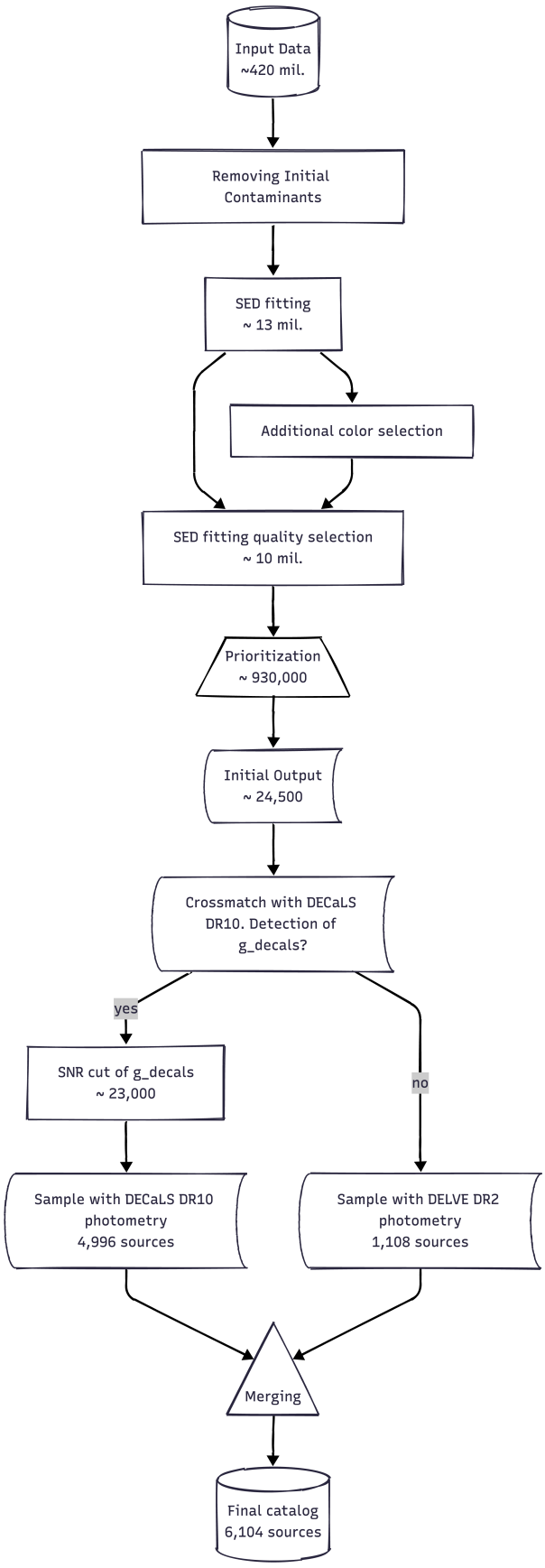

Fig. 1: Flowchart of selection procedure.

[2] `https://gal-04.voxastro.org/allsky_2022/`

[3] The sample is based on West et al. 2011, Lodieu et al. 2014, Mace 2014, Marocco et al. 2015 and Best et al. 2015

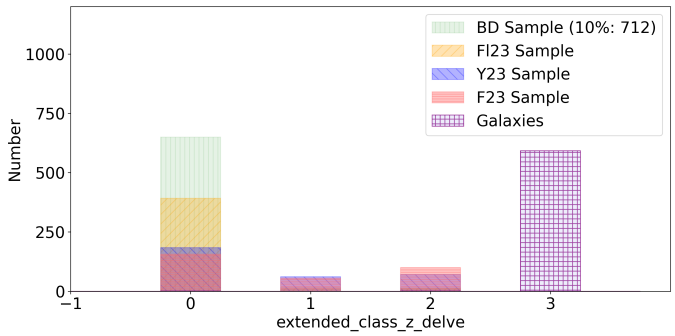

Fig. 2: DELVE *extended_class_z_delve* flag for samples of known high-redshift quasars, randomly selected brown dwarfs from the BD sample, and galaxies from the literature. The definition and usage of this flag are described in Section 3.1.

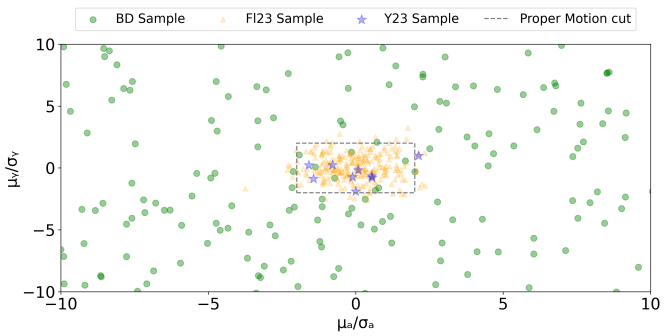

Fig. 3: Proper-motion significance in declination ($|\mu_\delta/\sigma_\delta|$) versus right ascension ($|\mu_\alpha/\sigma_\alpha|$) for various source types. BD sample is shown in green, while quasars from Y23 and Fl23 are plotted in blue and orange, respectively. The dashed box outlines the proper-motion cut applied in our analysis.

likelihood of being a star; 1: source is probably a star; 2: source is likely a galaxy; 3 source has a high likelihood of being a galaxy. Therefore, we excluded all sources with an *extended_class_z_delve* value of 3, removing obvious extended sources from our dataset. This selection process leads to approximately a 33% reduction of the initial sample and successfully recovers over 98% of the high-redshift quasars from all reference samples used. We apply this method to a galaxy sample obtained from the SDSS SkyServer DR10[4] and find that this criterion eliminates 97% of them (see Figure 2).

As high-redshift quasars are not expected to show large proper motion (Heintz et al. 2018), we eliminated all sources with significant proper motions relative to their measurement uncertainties with the following cut to all sources with matches to Gaia DR3:

$$\left|\frac{\mu_\alpha}{\sigma_{\mu_\alpha}}\right| > 2 \quad \text{or} \quad \left|\frac{\mu_\delta}{\sigma_{\mu_\delta}}\right| > 2, \tag{1}$$

where μ_α and μ_δ are the proper motions in RA and Dec, respectively, and σ_{μ_α} and σ_{μ_δ} are their corresponding uncertainties.

The 2σ threshold provides an optimal balance between quasar completeness and contamination control, as validated by previous studies of high-redshift quasar selection (Heintz et al. 2018). Thus, with this filter from the sources with matches in Gaia DR3 we retain only 8% of the BD sample, preserving more than 93% of the known high-redshift quasars from Y23 and Fl23. No Gaia DR3 counterparts were found for sources in the F23 sample in this analysis (see Figure 3).

[4] `https://skyserver.sdss.org/dr10/en/tools/toolshome.aspx`

We also excluded all objects with g_{delve} detection, as we aim to select high-redshift quasars at $z > 4.5$. Instead, we retained objects with a g_{delve} value of 0 or 99, which may indicate either a lack of detection in the g band or no information. With this cut, we removed 76% of known brown dwarfs, while retaining over 97% of known quasars from the F23 and Y23 samples.

Finally, MIR color selection using simple WISE color cuts has been shown to be an effective method for identifying AGNs (e.g., Stern et al. 2012, DiPompeo et al. 2015, Secrest et al. 2015, Assef et al. 2018). We applied the following cut on WISE colors in AB:

$$W1 - W2 < 0.6 \quad \text{and} \quad W1 - W2 > -0.6. \tag{2}$$

This selection keeps over 76% of known high-redshift quasars matched with ALLWISE from the F23 sample while eliminating approximately 92% of known brown dwarfs (see Figure 4). This trade-off prioritizes quasar completeness over brown-dwarf rejection, as brown dwarfs significantly outnumber high-redshift quasars. At this stage, we are left with a sample of around 13 million sources, which we will refine further using SED fitting. Table 1 summarizes the results of the initial cuts performed on the test samples.

Table 1: Results from the initial cut procedure on known high-redshift quasars and brown dwarfs.

Conditions	F23	Y23	Fl23	BD
	Recovered	Recovered	Recovered	Remained
`Extended` z_{delve} cut	321 (99%)	318 (98%)	445 (99%)	3541 (91%)
`Proper motion` cut	—	222 (95%)	417 (93%)	407 (8%)
g_{delve} cut	321 (99%)	314 (97%)	188 (42%)	865 (24%)
`WISE color` cut	170 (76%)	152 (95%)	382 (85%)	604 (8%)

Notes. Numbers show recovered sources with recovery percentages in parentheses.

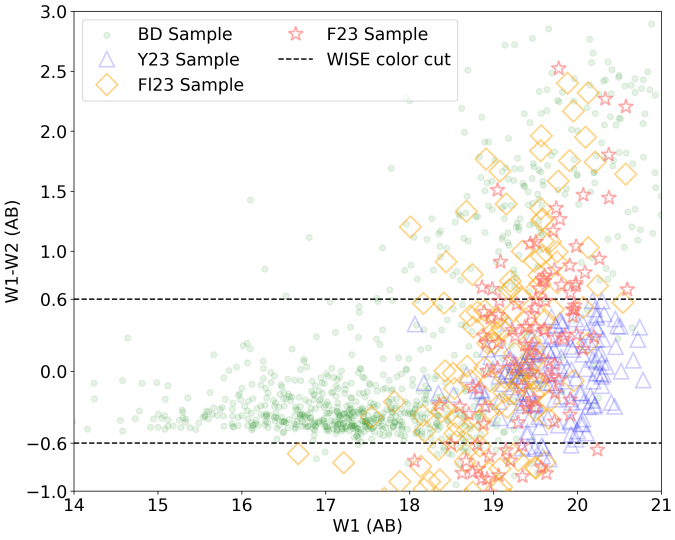

Fig. 4: The W1–W2 color criterion is applied to samples of known high-redshift quasars and brown dwarfs. This cut retains more than 76% of quasars while removing 92% of brown dwarfs.

3.2. SED fitting

After applying our initial cuts, we implemented a custom-made SED fitting code[5] to further refine the sample. As extended sources were substantially rejected in the previous step, the main contaminants at this stage are brown dwarfs. Indeed, the red flux profile of high-redshift quasars is due to significant absorption of the quasars' ultraviolet emissions by the IGM. On the other hand, brown dwarfs exhibit a gradually rising SED toward 1 µm due to their surface chemical composition and low temperature (e.g., Chiu et al. 2007). In this step, we used an SED fitting program with various templates. Quasar templates were sourced from Selsing et al. (2016) and Temple et al. (2021), while brown-dwarf templates are from Chung et al. (2014).

The template described in Selsing et al. (2016) is based on stacked spectra of luminous quasars observed by the SDSS at a redshift of $z \sim 3$. We shifted the observed template in a redshift range between 4.5 and 6.9, with increments of 0.1, and kept the redshift as a free parameter. We applied IGM absorption using the method outlined by Madau (1995). Additionally, we used a set of synthetic models from the `qsogen` code[6] from Temple et al. (2021). This model includes three free parameters: emission-line strength (weak, normal, and strong); dust reddening characterized by color excess values of $E(B-V) = 0, 0.1$, and 0.25 (where the extinction is attributed to dust within the quasar's host galaxy); and redshift. The redshifts of these synthetic templates range from 4.5 to 7, increasing in steps of 0.05. To account for contamination, four synthetic brown-dwarf templates of those used by Chung et al. (2014) were included, with two free parameters: surface temperature (2500 K, 2000 K, 1500 K, and 1000 K) and gravitational potential (log g = 5.15 and 4.90), based on models from Allard et al. (2007). The calculation of the synthetic photometry from all these templates was done with the `synphot` 1.2.1 python package[7].

We acknowledge that combining two quasar template sets may, in principle, introduce additional degeneracies; however, we note that $\sim 95\%$ of sources in our final catalog are best fit by the Temple et al. (2021) templates, which include the largest number of free parameters and provide the broadest coverage of quasar properties. The dominant contribution from a single template set therefore limits the practical impact of such degeneracies on our SED fitting quality.

We fit the observed SEDs by selecting the BD and quasar templates that minimize the χ^2. We then used the Bayesian information criterion (BIC) and F_{test} statistics to distinguish those significantly better fits as quasars. We calculated χ^2 as

$$\chi^2(z) = \sum_{i=1}^{N_{\rm filters}} \left[\frac{F_{{\rm obs},i} - b \times F_{{\rm temp},i})}{\sigma_i} \right]^2 , \tag{3}$$

where $F_{{\rm obs},i}$ and $F_{{\rm temp},i}$ represent the observed and template fluxes, σ_i is the flux uncertainty in the filter i, and b serves as a normalization factor. This normalization factor accounts for the flux normalization of template spectra and ensures optimal matching between observed and template photometry before χ^2 calculation.

We calculated the BIC as

$$BIC = \Delta \min \chi^2 + n_{\rm par} \Delta \times \ln(N_{\rm datapoint}), \tag{4}$$

where $\Delta \min \chi^2$ is the difference between the minimum χ^2 value of the brown dwarf and quasar templates, $n_{\rm par}\Delta$ is the difference between the numbers of parameters of the brown dwarf and quasar templates, and $N_{\rm datapoint}$ is the sum of data points of the source, where a datapoint is the flux in each filter.

We used a simplified version of the canonical F_{test} parameter in this study, resulting in the following expression:

$$F_{test} = \frac{\left|\min \chi^2 \Delta\right| \times k}{n_{\rm par}\Delta \times \min \chi^2}, \tag{5}$$

where (k) is the degree of freedom,

$$k = N_{\rm datapoint} - (n_{\rm par\ model} + n_{\rm par}\Delta) , \tag{6}$$

and $n_{\rm par\ model}$ is the number of parameters of the applied quasar template.

Before performing the SED fitting on our full catalog, we first validated our method using the set of known quasars and brown dwarfs. We assessed if the photometric redshift (z_{phot}) estimates are suitable for subsequent color selection by comparing them to spectroscopic redshifts (z_{spec}) for known quasars and, most importantly, whether the method successfully distinguishes between quasars and brown-dwarf contaminants by examining the ratio of best-fit χ^2 values (e.g., Ahumada et al. 2020 and Fan et al. 2023) (see Figure 5 for an example).

[5] The SED fitting code is publicly available via github: `https://github.com/dathevik/high-z-qso-selection.git`.
[6] `https://github.com/MJTemple/qsogen/`.
[7] `https://synphot.readthedocs.io/en/latest/`.

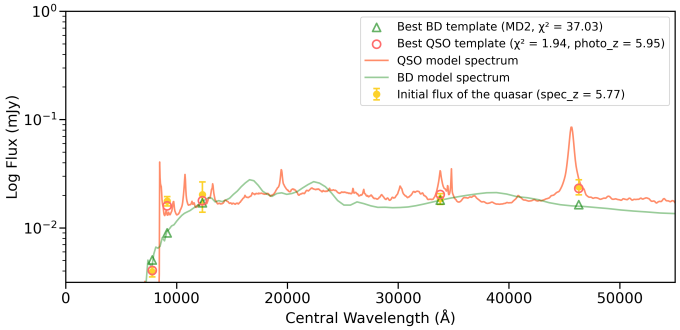

Fig. 5: Example of SED fitting for the known quasar $J000009.99-041626.09$ from the F23 sample ($z_{spec} = 5.77$, $z_{phot} = 5.95$).

3.3. Additional color selection

At this stage, following the SED fitting step, we had approximately 13 million candidates. We used the SED-calculated z_{phot} to perform additional color-based selection this time with $r_{delve} - i_{delve}$ colors from DELVE. We used the color distribution of known high-redshift quasars from the F23 sample to determine the optimal threshold for the $r_{delve} - i_{delve}$ bands and find that sources at $z_{spec} > 4.5$ systematically exhibit $r_{delve} - i_{delve} > 1.3$ (see Figure 6). Therefore, for objects with $z_{phot} < 6$, we imposed a color cut of $r_{delve} - i_{delve} > 1.3$. Because of the small number of sources (178) at $z_{phot} > 6$ in our sample, the color cut was only performed on the sources with $z_{phot} < 6$, while all the sources with $z_{phot} > 6$ were retained without applying color cuts. This cut removed approximately 3 million sources, retaining 10 million for further cuts.

3.4. SED-fitting quality selection

At this stage, we considered the χ^2, BIC, and $F_{\rm test}$ values obtained from our SED fitting from the F23 and BD samples (see Figure 7). To test the effectiveness of each criterion, we tested them separately on known brown dwarfs: $BIC > 0$ alone removed around 57%, while $F_{\rm test} > 10$ alone removed approximately 99% of the BD sample. In our selection pipeline, we applied both criteria simultaneously to maximize contaminant rejection. Additionally, to ensure we selected candidates with reliable and genuinely multiwavelength photometry, we required sources to have detections in seven or more photometric bands, which typically guarantees coverage across all three surveys or across two surveys with substantial photometric information. For sources with 7–8 bands, missing data were most commonly due to the gaps in VHS/VIKING fields in H or Y bands, and more rarely in the DELVE r-band coverage.

To summarize, we required

- $BIC > 0$ and $F_{test} > 10$,
- $N_{\rm datapoint} > 6$.

3.5. Prioritization

At this stage, we had narrowed our sample to approximately 930000 candidates. After performing morphology, color, SED-fitting, and related cuts, we prioritized sources

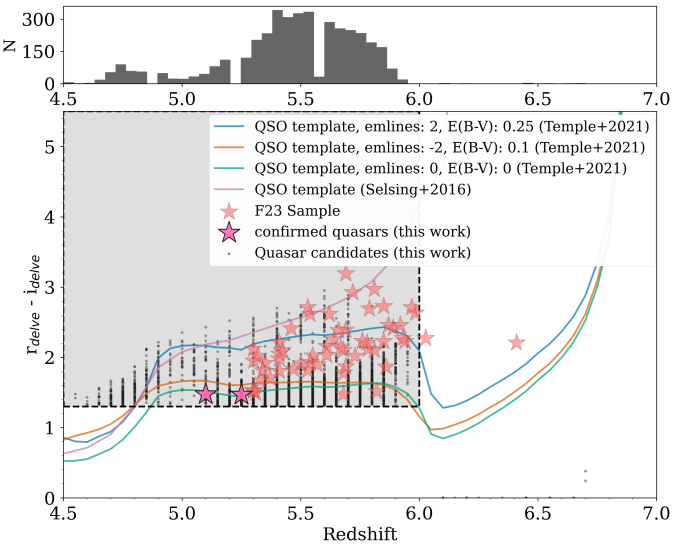

Fig. 6: Relation between $r_{delve} - i_{delve}$ color and redshift for high-redshift quasars from the F23 sample, using DELVE photometry, and our quasar candidates (this work), marked as small gray dots. The histogram at the top shows the distribution of SED-based photometric redshifts of our quasar candidates. The shaded gray area indicates the selection region defined by the criterion $r_{delve} - i_{delve} > 1.3$, which was applied to sources at $z_{phot} < 6$. All sources at $z_{phot} > 6$ are retained regardless of their color. The confirmed quasars from this work are shown as large pink stars.

for follow-up spectroscopy based on their brightness, their respective $\chi^2_{\rm QSO,min}$, and R_χ values defined as

$$R_{\chi^2} = \frac{\chi^2_{\rm QSO,min}}{\chi^2_{\rm BD,min}}, \tag{7}$$

where $R_{\chi^2} < 1$ indicates a better fit with quasar templates than brown-dwarf templates. This criterion alone removes 56% of known brown dwarfs while preserving more than 94% of known quasars.

We prioritized our candidates according to the following criteria:

- Priority 2: $z_{\rm delve} \leq 22$
- Priority 1: $z_{\rm delve} \leq 22$ and $\chi^2_{\rm QSO,min} \leq 1.2$ and $R_{\chi^2} \leq 0.3$.

Additionally, sources within 5° of the Large Magellanic Cloud and 2.5° of the Small Magellanic Cloud were excluded to avoid crowded regions, and the sample was restricted to declinations between −80° and 5° in order to focus on observable targets (Bauer et al. in prep). After this cut, we narrowed our initial output catalog down to approximately 24,500 sources with priorities 1 and 2.

3.6. Sample with DECaLS DR10 photometry

We cross-matched the remaining ∼24,500 sources with the DECaLS DR10 catalog via the NOIRLab Datalab interface[8] to obtain further photometric information. Of these, over 23000 have counterparts in g_{decals}. We applied a 3σ

[8] https://datalab.noirlab.edu

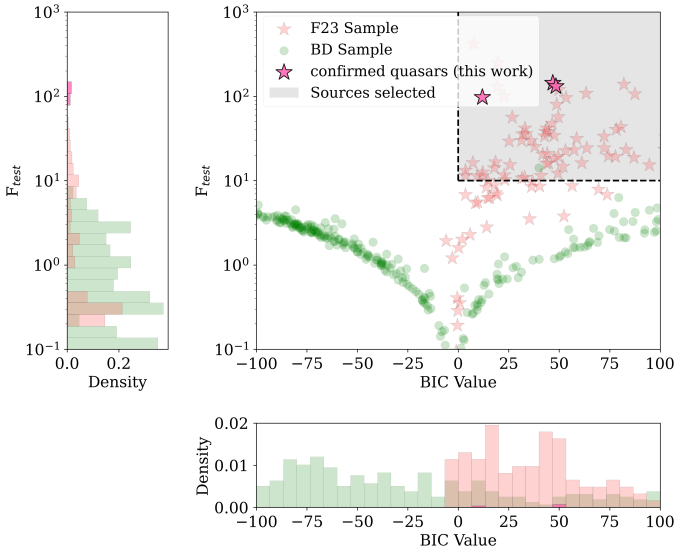

Fig. 7: Distribution of F_{test} and BIC values of high-redshift quasars from the F23 sample, the BD sample, and the spectroscopically confirmed high-redshift quasars from our sample. The shaded gray area indicates the selection region defined by our criteria ($BIC > 0$ and $F_{test} > 10$). The subplots indicate the density histogram of the corresponding axis.

detection-threshold criterion, which reduced our candidate list to 4996 objects. This was motivated by the fact that quasars at $z > 4.5$ are not expected to be detected in the g band due to Lyman-break absorption, and that the deeper g-band photometry of DECaLS DR10 ($g_{decals} = 24.7$) compared to DELVE DR2 ($g_{delve} = 24.3$) provides a strict criterion for excluding low-redshift contaminants with $g - band$ detections. As a result, we adopted DECaLS photometry for sources with the signal-to-noise (S/N) of $g_{decals} < 3$ and kept DELVE DR2 magnitudes for 1108 candidates without matches in DECaLS DR10 due to the incomplete sky coverage of DECaLS DR10. This approach led to two samples being created: one containing $griz$ bands from DELVE DR2 and the other from DECaLS DR10 selected based on the S/N of g_{decals} (see Figure 1 for the complete selection layout). Our final catalog of high-redshift quasar candidates, which will be observed within ChANGES, includes 6104 sources in total, 58% of which are priority 1 sources.

4. Results

Our main aim is to identify a sample of high-redshift quasar candidates for the ChANGES survey. In Figure 8, we report the distribution of the minimum χ^2 values obtained from SED fitting with quasar templates for our final catalog, which includes sources classified as both priority 1 and priority 2 candidates (see Section 3.5). Given that all sources in the sample are required to have photometric information in seven or more filters and that the fitting procedure involved either three or one free parameter(s), depending on the best fitting template, the expected acceptable range for total χ^2 values is approximately between four and 14. This corresponds to reduced χ^2 values (i.e., $\chi^2_\nu = \chi^2/\nu$, where ν is the number of degrees of freedom) ranging from ∼1 to ∼5, where lower values indicate statistically better fits.

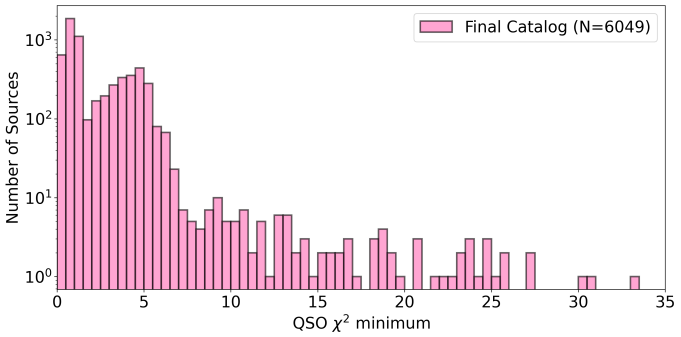

Fig. 8: $\chi^2_{\rm QSO,min}$ distribution of the final catalog of 6104 high-redshift quasar candidates. The distribution shows the first sharp peak near $\chi^2_{\rm QSO,min} \sim 1$ due to the performed prioritization cuts.

To test the completeness of our sample of high-redshift quasar candidates, we chose all the available sources in declinations between −30° and 0° to obtain the highest number of known high-redshift quasars from samples of F23. As a control variable, we kept the sources with $z_{\rm delve} < 22$. The completeness and reliability were estimated using the following formulas:

$$C = \frac{\text{Number of selected quasars}}{\text{Total number of confirmed quasars}}, \quad (8)$$

where completeness (C) measures how well our selection method recovers known quasars from the total population of confirmed quasars from the F23 sample in our selected region; and

$$R = \frac{\text{Number of selected quasars}}{\text{Total number of selected objects}}, \quad (9)$$

where reliability (R) quantifies the fraction of our selected candidates that are quasars, providing a measure of contamination in our sample.

With this approach, we reached 44% completeness and 1.5% reliability (see Figure 9). Here, reliability is computed as the fraction of our selected candidates that are spectroscopically confirmed quasars from the F23 sample; the remaining candidates have not been spectroscopically confirmed and should not be assumed to be contaminants. The pink points in the top panel of Figure 9 represent our unconfirmed quasar candidates. Therefore, given the incompleteness of southern-sky spectroscopic samples, the measured reliability should be interpreted as a conservative lower limit rather than a definitive estimation of our selection's true performance. A full assessment of completeness and reliability would require modeling the selection function to quantify the impact of each selection criterion, which is deferred to future work after dedicated spectroscopic follow-up.

As part of our validation efforts, six high-redshift quasar candidates from our final catalog were observed spectroscopically. Initial observations of three candidates were conducted with the New Technology Telescope (NTT) at La Silla Observatory during ESO program ID 115.2816.001 between UT 2025 July 27 and August 2. The observations were conducted using the ESO Faint Object Spectrograph

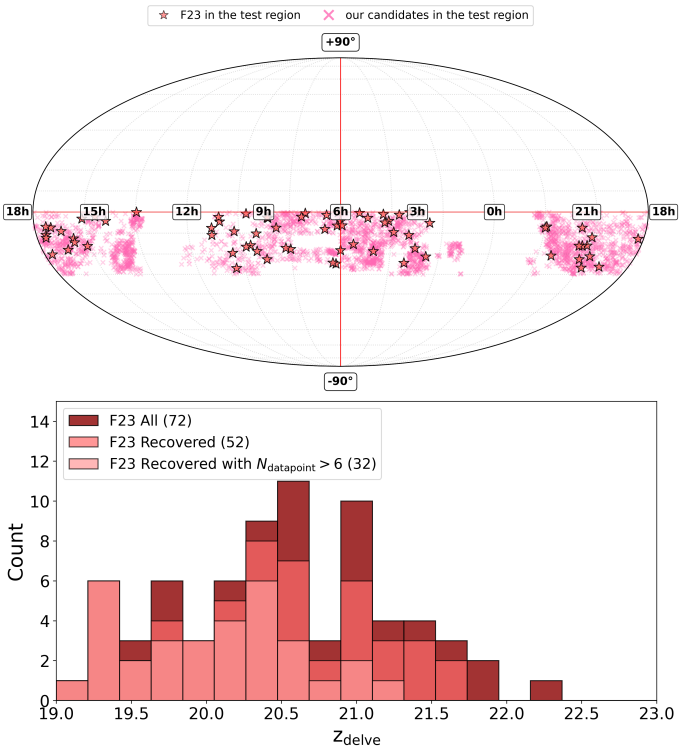

Fig. 9: Distribution of sources from F23 sample and our final catalog within the declination range $-30° < \text{Dec} < 0°$. Top panel: Sky distribution of the selected region for our candidates of high-redshift quasars with high-redshift quasars from the F23 sample. Bottom panel: Histogram of z_{delve} for the F23 sample in the selected region and with respect to the ones recovered after the selection procedures with and without limiting the $N_{\text{datapoint}}$.

and Camera (v.2; EFOSC2 Buzzoni et al. 1984) with the Grism 5 (5200–9350 Å), which provided spectral coverage suitable for confirming high-redshift quasars by detecting the Lyman break. The observing run faced challenges due to poor weather conditions, with variable seeing ranging from $1.1 - 1.8''$ and intermittent cloud cover. One source (`Name:`$J2248 - 1803$, $z_{delve} = 19.95$) showed a promising Lyman break at $z \sim 5.6$, representing a potential high-redshift quasar. The other two targets (`Name:`$J2223 - 1042$ and $J2228 - 1650$) were identified as contaminants: one is a low-redshift ($z \sim 3.2$) source, and the other showed inconclusive results. The data for all sources were reduced with standard routines (e.g., Belladitta et al. 2025) using the `PypeIt` pipeline[9] (Prochaska et al. 2020). Given the promising but very low S/N NTT/EFOSC2 spectrum of J2248-1803 and the poor observing conditions (seeing up to $1.8''$), further follow-up observations were conducted with the Palomar Observatory using the Next Generation Palomar Spectrograph (NGPS; Jiang et al. 2018) on UT 2025 August 23. The spectrum of the source clearly shows the characteristic Lyman break at $\sim$ 8000 Å, confirming the quasar at a spectroscopic redshift of $z_{spec} = 5.606$, which is consistent with the photometric redshift estimate from our SED fitting analysis. Following the confirmation of J2248-1803, three additional candidates were observed with Palomar/NGPS. The Palomar/NGPS spectra were reduced using standard IRAF routines. Of these three targets, two were successfully confirmed as high-redshift quasars (see Figure 10). The third target (Object ID 10735100050971) is likely an M-type star (see Table 2). Overall, our spectroscopic campaign achieved a detection rate of 50% (3 confirmed quasars out of 6 observed candidates). However, we note that this rate is not representative of the full catalog, as these candidates were specifically selected based on their brightness and a visual inspection. The true reliability of our selection will be determined once spectroscopic information is obtained for the entire catalog. It is important to note that all these sources were selected from our catalog of high-redshift quasar candidates based on their z-band magnitudes ($z_{mag,decals} < 20.5$). We also visually inspected their images in the Legacy Survey Sky Viewer and PanSTARRS-1 Image Access to prioritize bright and clear point-like sources.

[9] `https://pypeit.readthedocs.io/en/stable/`

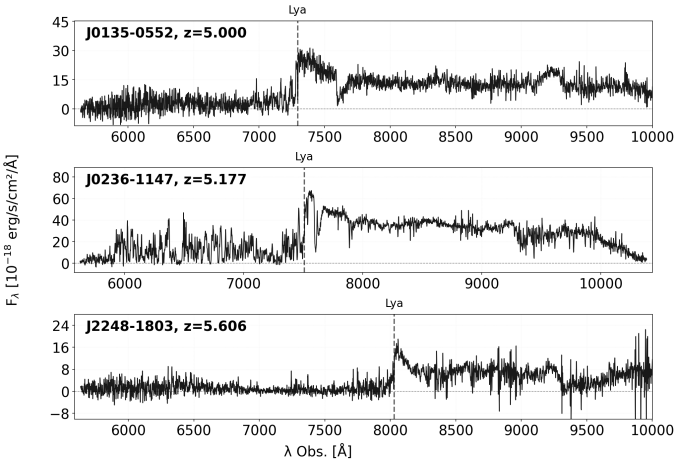

Fig. 10: Palomar/NGPS spectrum of the three confirmed high-redshift quasars, observed on UT 2025 August–November. The spectra show the Lyman-α break (indicated by the vertical dashed line), confirming the quasar nature for those candidates selected through our SED fitting methodology.

5. Summary

In this work, we developed multistep selection procedures to identify high-redshift quasar candidates for spectroscopic follow-up as part of the 4MOST ChANGES survey. Starting from a cross-matched catalog of $\sim$ 420 million sources across the southern hemisphere, we applied a series of morphological, color-based, and statistical criteria, followed by custom-built SED fitting using empirical and theoretical templates for both quasars and brown dwarfs. Our initial filtering reduces the candidate list to approximately 25,000 sources, from which a final catalog of 6104 candidates was created (see Figure 11).

As shown in Table 3, the sequential application of selection criteria significantly narrowed the candidate pool. For example, the color-color selection ($r_{delve} - i_{delve} > 1.3$ criterion applied in Section 3.3) retains a large fraction of known quasars (e.g., 100% for the F23 sample). However, subsequent steps, including the data-quality require-

Table 2: Information on the six high-redshift quasar candidates spectroscopically followed up with NTT/EFOSC2 and Palomar/NGPS.

Name	RA (deg)	Dec (deg)	g_{decals} (AB mag)	r_{decals} (AB mag)	i_{decals} (AB mag)	z_{decals} (AB mag)	χ^2_{QSO}	R_{χ^2}	z_{phot}	z_{spec}	Exp. Time (s)	Seeing (arcsec)	Telescope/Instrument
$J2228-1650$	337.0605	-16.8485	—	—	19.97 ± 0.010	19.71 ± 0.013	0.589	0.013	5.350	—	1800	1.2	NTT/EFOSC2
$J2248-1803$	342.1769	-18.0430	26.99 ± 2.38	—	20.79 ± 0.015	19.96 ± 0.018	2.048	0.012	5.650	5.606	1800	1.2	Palomar/NGPS
$J2109-2639$	317.4431	-26.6500	—	—	20.28 ± 0.016	19.85 ± 0.020	1.471	0.030	5.150	—	1800	1.2	NTT/EFOSC2
$J0135-0552$	23.7621	5.8731	25.90 ± 0.27	21.70 ± 0.05	20.17 ± 0.02	20.00 ± 0.02	1.354	0.027	5.100	5.000	1200	1.3	Palomar/NGPS
$J0237-1148$	39.2023	11.7926	26.97 ± 0.27	20.22 ± 0.03	18.75 ± 0.01	18.45 ± 0.01	1.527	0.029	5.250	5.177	1200	1.0	Palomar/NGPS
$J2223-1042$	335.7022	10.7067	25.10 ± 0.15	23.23 ± 0.10	—	20.41 ± 0.03	2.138	0.029	6.100	—	1200	1.0	Palomar/NGPS

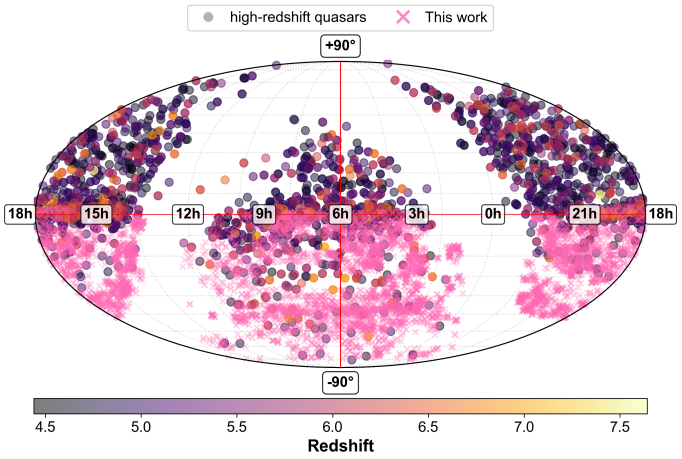

Fig. 11: Spatial distribution of high-redshift quasar candidates in the southern hemisphere. Pink crosses show our candidates, while darker points are spectroscopically confirmed high-redshift quasars from the literature (F23, Y23, and Fl23 samples). The deficit around RA $\sim 120°$–$240°$ results from increased Galactic extinction and our $E(B-V) < 0.3$ selection criterion. This distribution aligns well with the ChANGES survey strategy, which targets $\sim 18,000$ deg^2 across declinations between $-80°$ and $+5°$ to maximize overlap with future LSST observations and match 4MOST's optimal observing range.

ments (described in Section 3.4) and the $E(B-V) < 0.3$ dust-extinction cut, reduced the retained sample to below 40% across the known high-redshift quasar samples. The prioritization criteria (Section 3.5) further refined the ∼930000 remaining candidates by ranking them on brightness and SED fit quality, recovering 7–8% of known quasars in the higher confidence tier. Finally, the $N_{\rm datapoint} > 6$ requirement, which is also part of the quality selection in Section 3.4, ensured reliable multiwavelength coverage, reducing the recovered fractions to 26–37%. We note that the $N_{\rm datapoint}$ and $z_{\rm delve}$ brightness cuts served as data-quality filters rather than astrophysical discriminators and are therefore listed below the dashed line in Table 3.

The performance of our selection methodology can be assessed through three key metrics: recovery rate, completeness, and reliability. Our recovery rates from known high-redshift quasar samples (see Table 3) demonstrate that 7–8% of confirmed quasars were retained after our complete selection process. Our completeness assessment, focusing on sources with optimal data quality in the $-30° < Dec < 0°$ declination range, yields 44% recovery of known quasars, indicating that our selection criteria identify a substantial fraction of the existing high-redshift quasar population. The reliability of our sample, defined as the fraction of selected candidates that are quasars without imposing the $N_{datapoint} > 6$ requirement, reaches 1.5% in our test region. Assuming a similar population in our target field, and considering that our input catalog contains over 6,000 candidates, we expect to identify about 7% of high-redshift quasars. However, this estimate should be approached with caution, as the actual number depends on the properties of the sources within the observed field and how representative the comparison catalogs are.

The spectroscopic observations of this catalog with 4MOST will be finalized in the coming years. It consists of 44 parameters (see Table 4), including magnitudes across various photometric bands, statistical results from the SED fitting, and $E(B-V)$ values from SFD maps.

Table 3: Results of selection process to identify high-redshift quasars and brown dwarfs.

Conditions	F23 Recovered	Y23 Recovered	Fl23 Recovered	BD Remained
Color-color selection	100%	96%	32%	98%
$BIC > 0$ and $F_{test} > 10$	70%	39%	65%	0.004%
$E(B-V) < 0.3$	70%	38%	70%	0.004%
Priority 1	7%	8%	9%	—
Priority 2	65%	38%	94%	0.001%
$N_{datapoint} > 6$	37%	28%	26%	0.0008%

Notes. The percentages indicate the fraction of sources retained after each selection criterion with respect to the total number of detected sources. See Section 3 for more details and references for each sample. The selection criteria above the dashed line represent the core scientific filters based on statistical, morphological, and color criteria, achieving recovery rates of 70% for high-redshift quasars in the F23 sample (with 7% being higher priority sources) and 38% for the Y23 sample (with 8% being higher likelihood sources) and 18% for the Fl23 sample (with 9% being higher likelihood sources). The criteria below the dashed line ($z_{\rm delve}$ cut for Priority 2 and $N_{\rm datapoint}$) were applied to ensure high data quality. They were not included in the final recovery rate calculations as they filter for source trustworthiness rather than astrophysical properties.

Data availability

The full catalog of high-redshift quasar candidates is only available in electronic form at the CDS via anonymous ftp to `cdsarc.u-strasbg.fr` (130.79.128.5) or via `http://cdsweb.u-strasbg.fr/cgi-bin/qcat?J/A+A/`.

Acknowledgements. We thank the anonymous referee for their valuable suggestions, which improved the quality of this paper. We also thank the journal editor for their time, effort, and careful coordina-

Table 4: Column-by-column description of the high-redshift quasar-candidate catalog.

Column	Description
`object_id`	ID number of the source taken from DELVE DR2
`ra`, `dec`	Right ascension and declination (degrees) taken from DELVE DR2
`mag_g_delve, ..., mag_z_delve`	AB Kron magnitudes taken from DELVE DR2 by default
`msgerr_g_delve, ..., ,magerr_z_delve`	Magnitude errors from DELVE DR2
`mag_g_decals, ..., mag_z_decals`	AB Kron magnitudes taken from DECaLS DR10 photometry
`snr_g_decals, ..., snr_z_decals`	S/N from DECaLS DR10
`ypetromag, ..., kspetromag`	YJHKs Petrosian magnitudes from VHS
`ypetromagerr, ..., kspetromagerr`	YJHKs magnitude errors from VHS
`w1mpro, w2mpro, w1sigmpro, w2sigmpro`	WISE W1 and W2 magnitudes and errors
`BD_chi2_min`, `BD_chi2_template`	$\chi^2_{\rm BD,min}$ for brown-dwarf templates and best-fit BD template type
`QSO_chi2_min`, `QSO_z`	$\chi^2_{\rm QSO,min}$ value for quasar templates and photometric redshifts
`R_chi2`	QSO to BD χ^2 ratio; < 1 means QSO fit is better
`F_test_value`	F-test values
`BIC_value`	Bayesian Information Criterion values
`QSO_EBV`, `QSO_EMline`, `QSO_Par`	QSO template parameters
`Data_Points`	Number of bands used in the fit
`ebv`	Galactic $E(B-V)$ from SFD maps
`Prioritization`	Prioritization of the sources based on $\chi^2_{\rm QSO,min}$ and R_{χ^2}

tion of the refereeing process. We acknowledge support from Fondecyt Iniciación grant 11240336 (TM, CM), the ANID BASAL project FB210003 (TM, CM, RJA, ARL, FEB, LNMR, SSS), Fondecyt Regular grant 1231718 (RJA), Fondecyt Regular grant 1241005 (FEB, LNMR), Millennium Science Initiative, AIM23-0001 and ICN12_009 (FEB, LNMR), the National Agency for Research and Development (ANID) under the fellowship ANID Becas/Doctorado Nacional#21220337 (LNMR-R) and the Vicerrectoría de Investigación of Pontificia Universidad Católica de Chile under the fellowship Stay of Doctoral Co-tutelage Abroad, leading to double degree (LNM-R). MJT acknowledges funding from a FONDECYT Postdoctoral fellowship (3220516) and from UKRI STFC (ST/X001075/1). The work of DS was carried out at the Jet Propulsion Laboratory, California Institute of Technology, under a contract with the National Aeronautics and Space Administration (80NM0018D0004). E.P.F. is supported by the international Gemini Observatory, a program of NSF NOIRLab, which is managed by the Association of Universities for Research in Astronomy (AURA) under a cooperative agreement with the U.S. National Science Foundation, on behalf of the Gemini partnership of Argentina, Brazil, Canada, Chile, the Republic of Korea, and the United States of America. This work is part of the 4-meter Multi-Object Spectroscopic Telescope (4MOST) Chilean AGN/Galaxy Extragalactic Survey (ChANGES) collaboration, and we acknowledge the support of the ChANGES team. We are grateful to the ESO staff at La Silla Observatory for their support during the NTT/EFOSC2 observations under program 115.2816.001, and to the Palomar/NGPS observations, which confirmed three high-redshift quasar candidates. This work is based on data from the Dark Energy Camera Local Volume Exploration Survey (DELVE DR2), the Dark Energy Camera Legacy Survey (DECaLS DR10), the VISTA Hemisphere Survey (VHS DR5), CatWISE 2020 catalog and Gaia DR3. We acknowledge using data products from the NOIRLab Datalab.

References

Abbott, T. M. C., Abdalla, F. B., Allam, S., et al. 2018, ApJS, 239, 18
Ahumada, R., Allende Prieto, C., Almeida, A., et al. 2020, ApJS, 249, 3
Allard, F., Allard, N. F., Homeier, D., et al. 2007, A&A, 474, L21
Assef, R. J., Stern, D., Noirot, G., et al. 2018, ApJS, 234, 23
Bañados, E., Carilli, C., Walter, F., et al. 2018, ApJ, 861, L14
Bañados, E., Schindler, J.-T., Venemans, B. P., et al. 2023, ApJS, 265, 29
Bañados, E., Venemans, B. P., Decarli, R., et al. 2016, ApJS, 227, 11
Bauer, F. E., Lira, P., Anguita, T., et al. 2023, The Messenger, 190, 34
Becker, G. D., Bolton, J. S., & Lidz, A. 2015, PASA, 32, e045
Belladitta, S., Bañados, E., Xie, Z.-L., et al. 2025, A&A, 699, A335
Belladitta, S., Moretti, A., Caccianiga, A., et al. 2023, A&A, 669, A134
Belladitta, S., Moretti, A., Caccianiga, A., et al. 2019, A&A, 629, A68
Bertin, E. & Arnouts, S. 1996, A&AS, 117, 393
Best, W. M. J., Liu, M. C., Magnier, E. A., et al. 2015, ApJ, 814, 118
Bogdán, Á., Goulding, A. D., Natarajan, P., et al. 2024, Nature Astronomy, 8, 126
Bosman, S. E. I., Davies, F. B., Becker, G. D., et al. 2022, MNRAS, 514, 55
Brandt, W. N., Alexander, D. M., Hornschemeier, A. E., et al. 2001, AJ, 122, 2810
Buzzoni, B., Delabre, B., Dekker, H., et al. 1984, The Messenger, 38, 9
Byrne, X., Meyer, R. A., Farina, E. P., et al. 2024, MNRAS, 530, 870
Calderone, G., Guarneri, F., Porru, M., et al. 2024, A&A, 683, A34
Chambers, K. C., Magnier, E. A., Metcalfe, N., et al. 2016, arXiv e-prints, arXiv:1612.05560
Champagne, J. B., Wang, F., Yang, J., et al. 2025a, ApJ, 981, 114
Champagne, J. B., Wang, F., Zhang, H., et al. 2025b, ApJ, 981, 113
Chiu, K., Richards, G. T., Hewett, P. C., & Maddox, N. 2007, MNRAS, 375, 1180
Chung, S. M., Kochanek, C. S., Assef, R., et al. 2014, ApJ, 790, 54
Davies, R. L., Ryan-Weber, E., D'Odorico, V., et al. 2023, MNRAS, 521, 289
de Jong, R. S., Agertz, O., Berbel, A. A., et al. 2019, The Messenger
Dey, A., Schlegel, D. J., Lang, D., et al. 2019, AJ, 157, 168
DiPompeo, M. A., Myers, A. D., Hickox, R. C., et al. 2015, MNRAS, 446, 3492
Drlica-Wagner, A., Ferguson, P. S., Adamów, M., et al. 2022, ApJS, 261, 38
Edge, A., Sutherland, W., Kuijken, K., et al. 2013, The Messenger, 154, 32
Euclid Collaboration, Barnett, R., Warren, S. J., et al. 2019, A&A, 631, A85
Fan, X., Bañados, E., & Simcoe, R. A. 2023, ARA&A, 61, 373
Fan, X., Narayanan, V. K., Lupton, R. H., et al. 2001, AJ, 122, 2833
Farina, E. P., Schindler, J.-T., Walter, F., et al. 2022, ApJ, 941, 106
Findlay, J. R., Sutherland, W. J., Venemans, B. P., et al. 2012, MNRAS, 419, 3354
Flaugher, B. 2005, International Journal of Modern Physics A, 20, 3121
Flesch, E. W. 2023, The Open Journal of Astrophysics, 6, 49
Gaia Collaboration, Brown, A. G. A., Vallenari, A., et al. 2016, A&A, 595, A2
Gaia Collaboration, Vallenari, A., Brown, A. G. A., et al. 2023, A&A, 674, A1
Giacconi, R., Zirm, A., Wang, J., et al. 2002, ApJS, 139, 369
Gloudemans, A. J., Duncan, K. J., Saxena, A., et al. 2022, A&A, 668, A27
Guiglion, G., Battistini, C., Bell, C. P. M., et al. 2019, The Messenger, 175, 17
Hatziminaoglou, E., Perez-Fournon, I., Polletta, M., et al. 2004, arXiv e-prints, astro
Heintz, K. E., Fynbo, J. P. U., Høg, E., et al. 2018, A&A, 615, L8
Hewett, P. C., Warren, S. J., Leggett, S. K., & Hodgkin, S. T. 2006, MNRAS, 367, 454
Ighina, L., Caccianiga, A., Moretti, A., et al. 2023, MNRAS, 519, 2060
Ighina, L., Caccianiga, A., Moretti, A., et al. 2025, A&A, 698, A158
Ivezić, Ž., Kahn, S. M., Tyson, J. A., et al. 2019, ApJ, 873, 111
Iwamoto, R., Matsuoka, Y., Imanishi, M., et al. 2025, ApJ, 979, 183
Jiang, H., Hu, Z., Xu, M., et al. 2018, in Society of Photo-Optical Instrumentation Engineers (SPIE) Conference Series, Vol. 10702, Ground-based and Airborne Instrumentation for Astronomy VII, ed. C. J. Evans, L. Simard, & H. Takami, 107022L
Jiang, L., McGreer, I. D., Fan, X., et al. 2016, ApJ, 833, 222
Keller, S. C., Schmidt, B. P., Bessell, M. S., et al. 2007, PASA, 24, 1
Kocevski, D. D., Finkelstein, S. L., Barro, G., et al. 2025, ApJ, 986, 126
Lambert, T. S., Assef, R. J., Mazzucchelli, C., et al. 2024, A&A, 689, A331
Lawrence, A., Warren, S. J., Almaini, O., et al. 2007, MNRAS, 379, 1599
Lehmer, B. D., Brandt, W. N., Alexander, D. M., et al. 2005, ApJS, 161, 21
Lodieu, N., Boudreault, S., & Béjar, V. J. S. 2014, MNRAS, 445, 3908
Mace, G. N. 2014, PhD thesis, University of California, Los Angeles
Madau, P. 1995, ApJ, 441, 18
Magorrian, J., Tremaine, S., Richstone, D., et al. 1998, AJ, 115, 2285
Marchesi, S., Civano, F., Salvato, M., et al. 2016, ApJ, 827, 150
Marconi, A. & Hunt, L. K. 2003, ApJ, 589, L21
Marocco, F., Eisenhardt, P. R. M., Fowler, J. W., et al. 2021, ApJS, 253, 8
Marocco, F., Jones, H. R. A., Day-Jones, A. C., et al. 2015, MNRAS, 449, 3651
Matsuoka, Y., Onoue, M., Kashikawa, N., et al. 2016, ApJ, 828, 26
Matthee, J., Naidu, R. P., Brammer, G., et al. 2024, ApJ, 963, 129
Mazzucchelli, C., Bischetti, M., D'Odorico, V., et al. 2023, A&A, 676, A71
McMahon, R. G., Banerji, M., Gonzalez, E., et al. 2013, The Messenger, 154, 35
McMahon, R. G., Banerji, M., Gonzalez, E., et al. 2021
Messias, H., Afonso, J., Salvato, M., Mobasher, B., & Hopkins, A. M. 2012, ApJ, 754, 120
Mignoli, M., Gilli, R., Decarli, R., et al. 2020, A&A, 642, L1
Mortlock, D. J., Patel, M., Warren, S. J., et al. 2012, MNRAS, 419, 390
Nakoneczny, S. J., Bilicki, M., Pollo, A., et al. 2021, A&A, 649, A81
Natarajan, P., Pacucci, F., Ricarte, A., et al. 2024, ApJ, 960, L1
Onken, C. A., Lai, S., Wolf, C., et al. 2022, PASA, 39, e037
Pons, E., McMahon, R. G., Simcoe, R. A., et al. 2019, MNRAS, 484, 5142
Prochaska, J., Hennawi, J., Westfall, K., et al. 2020, The Journal of Open Source Software, 5, 2308
Pudoka, M., Wang, F., Fan, X., et al. 2024, ApJ, 968, 118
Reed, S. L., McMahon, R. G., Martini, P., et al. 2017, MNRAS, 468, 4702
Richards, G. T., Fan, X., Schneider, D. P., et al. 2001, AJ, 121, 2308
Richards, G. T., Myers, A. D., Peters, C. M., et al. 2015, ApJS, 219, 39
Richards, G. T., Nichol, R. C., Gray, A. G., et al. 2004, ApJS, 155, 257
Salvato, M., Hasinger, G., Ilbert, O., et al. 2009, ApJ, 690, 1250
Schlegel, D. J., Finkbeiner, D. P., & Davis, M. 1998, ApJ, 500, 525
Secrest, N. J., Dudik, R. P., Dorland, B. N., et al. 2015, ApJS, 221, 12
Selsing, J., Fynbo, J. P. U., Christensen, L., & Krogager, J.-K. 2016, A&A, 585, A87
Shen, Y., Richards, G. T., Strauss, M. A., et al. 2011, ApJS, 194, 45
Stern, D., Assef, R. J., Benford, D. J., et al. 2012, ApJ, 753, 30
Temple, M. J., Hewett, P. C., & Banerji, M. 2021, MNRAS, 508, 737
Venemans, B. P., Bañados, E., Decarli, R., et al. 2015, ApJ, 801, L11
Wang, F., Yang, J., Fan, X., et al. 2021, ApJ, 907, L1
Wang, T., Elbaz, D., Schreiber, C., et al. 2016, ApJ, 816, 84
Warren, S. J., Hewett, P. C., & Osmer, P. S. 1987, in Bulletin of the American Astronomical Society, Vol. 19, 1125
Wenzl, L., Schindler, J.-T., Fan, X., et al. 2021, AJ, 162, 72
West, A. A., Morgan, D. P., Bochanski, J. J., et al. 2011, AJ, 141, 97
Williams, R. E., Blacker, B., Dickinson, M., et al. 1996, AJ, 112, 1335
Wolf, C., Hon, W. J., Bian, F., et al. 2020, MNRAS, 491, 1970
Wright, E. L., Eisenhardt, P. R. M., Mainzer, A. K., et al. 2010, AJ, 140, 1868
Yang, D.-M., Schindler, J.-T., Nanni, R., et al. 2024, MNRAS, 528, 2679
Yang, J., Fan, X., Gupta, A., et al. 2023, ApJS, 269, 27
Yang, J., Wang, F., Fan, X., et al. 2020, ApJ, 897, L14
York, D. G., Adelman, J., Anderson, Jr., J. E., et al. 2000, AJ, 120, 1579